Additive Manufacturing 29 (2019) 100807

Contents lists available at ScienceDirect

Additive Manufacturing

journal homepage: www.elsevier.com/locate/addma

Full Length Article

An investigation into specimen property to part performance relationships for laser beam powder bed fusion additive manufacturing

Rakish Shrestha[a,b], Nima Shamsaei[a,b,*], Mohsen Seifi[c], Nam Phan[d]

[a] Department of Mechanical Engineering, Auburn University, Auburn, AL, 36849, USA
[b] National Center for Additive Manufacturing Excellence (NCAME), Auburn University, Auburn, AL, 36849, USA
[c] ASTM International, Washington, DC, 20036, USA
[d] Structures Division, Naval Air Systems Command (NAVAIR), Patuxent River, MD, 20670, USA

ARTICLE INFO

Keywords:
Fatigue
Melt pool
Specimen property
Part performance
Porosity

ABSTRACT

The influence of part size and geometry on the melt pool size, microstructural features, and resulting mechanical properties of additive manufactured 17-4 precipitation hardening (PH) stainless steel (SS), fabricated using a laser beam powder bed fusion (LB-PBF) process is investigated. Three different types of geometries including a dog-bone part (i.e. representing the specimen or the witness coupon) and two square rods with different cross-sectional sizes (i.e. representing the parts) were designed and fabricated using the same set of process parameters. Mechanical properties were determined under quasi-static tensile and uniaxial strain-controlled fully-reversed fatigue loading conditions. Experimental results confirmed a minimal effect of part geometry on the tensile behavior of the LB-PBF 17-4 PH SS as the yield strength ranged from 1145 to 1198 MPa and ultimate tensile strength varied from 1171 to 1231 MPa. On the other hand, part geometry had a significant impact on the fatigue behavior in the high cycle regime. Specimens fabricated from the large square blocks contained the lowest amount of porosity, and consequently, exhibited the highest fatigue resistance. On the contrary, the highest amount of porosity was observed in the specimens fabricated from the dog-bone parts resulting in an inferior fatigue resistance as compared to other geometries. Microstructural analysis was performed to estimate the effect of part geometry on the thermal history experienced during manufacturing by measuring the melt pool dimensions. Some effects of geometry on the melt pool dimensions were observed as the melt pool depth was found to be shorter for dog-bone specimens and longer for large block specimens. The less elongated melt pools in dog-bone specimens can be attributed to higher cooling rate experienced by the specimens resulting in more entrapped gas pores.

1. Introduction

The ability of additive manufacturing technology to fabricate parts with complex geometries and even assemblies has attracted significant attention from aerospace, biomedical, and automotive industries alongside various academic and governmental institutions. Despite various advantages of this emerging technology, additive manufactured (AM) parts are susceptible to inherent defects such as entrapped gas pores and lack of fusion (LoF) [1–4]. Distribution and quantity of such defects can be affected by the thermal history experienced during the manufacturing process, which in turn is a function of process parameters (e.g. laser power, hatch spacing, layer thickness, etc.) and design parameters (e.g. part geometry and build orientation) [5–7]. As a result, the effects of process and design parameters on defect distribution and ultimately mechanical properties of AM parts, specifically under fatigue loading, need to be investigated.

Moreover, the partially known effect of design parameters on the thermal history, microstructure, defects, and mechanical properties causes significant challenges in standardization, qualification, and certification of AM parts [8]. For example, the relationships between small specimen properties measured in the laboratory to AM part performance under service loading should be determined before specimen properties can be used for qualification and certification of these parts [9,10]. Therefore, one is required to well understand how variations in design parameters, such as part size, geometry, and build orientation, affect the microstructural and mechanical properties and how the

Abbreviation: AM, Additive manufactured; CA, Condition A; HIP, Hot isostatic pressing; LB-DED, Laser beam directed energy deposition; LB-PBF, Laser beam powder bed fusion; LoF, Lack of fusion; PH, Precipitation hardening; SS, Stainless steel

* Corresponding author at: Department of Mechanical Engineering, Auburn University, Auburn, AL, 36849, USA.
E-mail address: shamsaei@auburn.edu (N. Shamsaei).

https://doi.org/10.1016/j.addma.2019.100807
Received 23 June 2019; Received in revised form 23 July 2019; Accepted 25 July 2019
Available online 30 July 2019

Nomenclature

$2N_f$	Reversals to failure
d_p	Melt pool depth
d_o	Overlap between consecutive melt pools
R_ε	Ratio of minimum to maximum strain
t_L	Layer thickness
ε_a	Strain amplitude
ε_f	Fracture strain
σ_a	Stress amplitude
σ_m	Mean stress
σ_y	Yield strength
σ_u	Ultimate tensile strength

process parameters can be adjusted for the specimens to be representative of the critical location of the part under service loading.

Several studies have been conducted to investigate the effects of various process parameters on the formation and distribution of different defect types. Cunningham et al. [11] investigated the effect of process parameters on the formation of different types of internal (i.e. volumetric) defects in Ti-6Al-4 V parts fabricated using laser beam powder bed fusion (LB-PBF) process and categorized them into LoF, keyholing, and entrapped gas pores. The LoF defects are recognized by their irregular shape and larger size ($> 100\,\mu m$) resulting from an insufficient overlap between adjacent layers or melt pools. Keyhole pores that are formed due to the vaporization of elements because of a high laser power and/or a low scan speed typically have more circular shape compared to the LoF. The entrapped gas pores resulting from the entrapment of gas pores in the melt pool are either present in the powder particles or come from the inert atmosphere. These types of defects typically have spherical morphology and smaller size as compared to the other two types (i.e. LoF and keyhole pores) [11].

Weingarten et al. [12] studied the formation of hydrogen entrapped gas pores as a function of scan speed in Al-Si-10Mg alloy fabricated using a LB-PBF process. An increase in scan speed was found to decrease the time between melting and solidification, resulting in less time for the hydrogen present as moisture in the powder to escape the melt pool, which causes the formation of entrapped gas pores [12]. Sheridan et al. [13] conducted a study to determine the distribution of porosity resulting from different scan patterns and variation in processing parameters including laser power, scan speed, and hatch spacing on the fatigue life of LB-PBF Inconel 718. First, they fabricated specimens using three types of meander scan strategies: continuous, stripe, and island. The smallest maximum pore size and longest fatigue lives were observed for specimens fabricated using the continuous meander scan strategy. For the second set of experiments, they fabricated specimens using a different combination of process parameters and reported the lowest porosity level and significantly better fatigue lives for specimens fabricated with higher scan speed and narrower hatch spaces [13].

On the other hand, studies on the effects of additive manufacturing design parameters on the distribution and formation of defects as well as the resultant mechanical properties have been mostly focused on the build orientation [14–17] and inter-layer time intervals [7,18]. For example, in a study conducted by Zhao et al. [19], a higher amount of porosity was reported for Al-Si-12Mg alloy fabricated in the horizontal direction compared to the vertical direction. Furthermore, irrespective to the build orientation, the fatigue life of LB-PBF Al-Si-12Mg was shown to primarily be governed by the size of the pores responsible for crack initiation. In the presence of similar size pores, the horizontally built specimens exhibited better fatigue resistance compared to the vertically built ones, which was attributed to the tendency of the cracks to propagate on the loading plane along the weakly bonded layers in the vertical specimens [19].

Similar observations were made in [16], in which a larger amount of LoF defects was noticed in the gage section of LB-PBF 17-4 PH SS specimens fabricated in horizontal direction compared to the ones built in vertical direction. Interestingly, even with the presence of a higher amount of defects, horizontal specimens exhibited better fatigue performance compared to the vertically built specimens. This anisotropy in the fatigue behavior was associated with the orientation of LoFs with respect to the loading direction. Due to the higher angle between the layer orientation (i.e. wide side of LoF defects) and the loading plane, higher stress concentrations are expected in vertical specimens as compared to the horizontal specimens. However, this anisotropic behavior may also depend on the type of defect initiating the fatigue crack, as the build orientation effect was minimum in LB-PBF Ti-6Al-4 V in the absence of LoF defects [20].

The orientation at which the specimens are fabricated can also result in the variation in heat dissipation within the same part and affect the formation of defects including surface roughness and pores. Pegues et al. [21] observed the surface roughness in LB-PBF Ti-6Al-4 V specimens fabricated at an angle of 45° to the built plate (i.e. diagonal direction) to be higher for the down-skin surface (i.e. surface facing the build plate) as compared to that of the up-skin surface (i.e. surface facing opposite to the build plate). The variation in the surface roughness was attributed to the difference in the volume of the solidified material available for the dissipation of heat during the fabrication of up-skin and down-skin surfaces. During the fabrication of up-skin surfaces, the majority of supplied heat is dissipated through the previously solidified layers. On the other hand, due to the smaller volume of solidified material available for the heat dissipation during the fabrication of down-skin surfaces, the specimen edge remains hotter for a longer period of time, which may result in a higher number of partially melted powder particles attached to the surface, and therefore, an increase in the surface roughness. Cracks in all specimens initiated from the down-skin surface with higher surface roughness. Similar results were also reported in [9] for LB-PBF Inconel 718, in which a higher surface roughness along with larger number of close-to-surface pores of down-skin surface of the diagonally fabricated parts initiated the crack in all specimens.

The effects of varying inter-layer time intervals on the mechanical properties and formation of defects in 316 L SS fabricated using a laser beam directed energy deposition (LB-DED) process were reported in [7]. To vary the inter-layer time interval, one cylindrical rod per build and multiple cylindrical rods per build were fabricated in vertical direction. Due to longer inter-layer time interval, multi-built specimens exhibited finer grains resulting in higher Vickers hardness, as well as yield and ultimate tensile strengths when compared to the specimens fabricated one at a time (i.e. single built). However, due to the higher inter-layer time interval, multi-built specimens contained higher amount of defects, resulting in them having a decreased elongation to failure. Similar results were also reported for Ti-6Al-4 V specimens fabricated using an LB-DED method in [18]. Shorter fatigue lives of the double-built specimens as compared to the single-built ones were related to the presence of large LoF defects in double-built specimens as compared to smaller spherical pores in single-built specimens.

The effects of design parameters including, build orientation and inter-layer time interval as well as process parameters, on the monotonic tensile and compressive properties of LB-PBF 17-4 PH SS were studied in [22]. Better yield and ultimate tensile strengths were reported for horizontally built specimens when compared to the vertically built specimens. Furthermore, the effect of inter-layer time interval for specimens fabricated in vertical direction was only seen to affect the hardness of the material, while other tensile properties were somewhat similar. This variation in hardness was associated with the discrepancies seen in the microstructure, resulting from differences in the

thermal history. Shorter time interval during the fabrication of single-built specimens resulted in a higher bulk temperature and lower cooling rate, leading to the presence of retained austenite, which decreased the hardness of LB-PBF 17-4 PH SS specimens. In the case of multi-built specimens, the longer inter-layer time interval resulted in lower bulk temperature, higher cooling rate, and presence of harder martensitic phase; thus, increasing the hardness value. Finally, the optimized process parameters obtained by decreasing the scan speed from 350 mm/s to 300 mm/s, while keeping the inter-layer time interval constant, was observed to improve the ultimate tensile strength and elongation to failure and result in smaller size pores and lower amount of porosity in the fabricated specimens [22].

Yang et al. [23] investigated the effects of energy per unit volume (volumetric energy density) and energy per unit area (areal energy density) on the formation of different types of defects including LoFs, small entrapped gas pores, and large keyhole pores for LB-PBF Al-7Si-Mg and Al-10Si-Mg alloys. Both volumetric and areal energy densities depended on the process parameters, mainly laser power, scan speed, and hatch spacing. The primary difference between the two types of energy densities was the consideration of layer thickness along with other parameters for calculation of volumetric energy density, while the layer thickness was excluded from calculation of the areal energy density. Results showed that a low volumetric energy density was responsible for formation of LoF defects, a high areal energy density was associated with the formation of small spherical entrapped gas pores, and a high volumetric energy density coupled with utilized meander scan strategy were responsible for larger key hole pores. The effect of part geometry on the distribution of defects was also investigated in [23] by fabricating a special type of specimen that consisted of cubic geometry at the bottom, cylinder in the middle section, and thin plate at the top. It was found that the thin plate section contained a higher level of porosity as compared to other two sections. This was attributed to the smaller cross-sectional area available in the thin plate for the heat to dissipate along with the use of meander scan pattern [23].

Therefore, formation and distribution of defects may be affected by changing the design parameters (e.g. part geometry, size or orientation), while keeping the process parameters constant. Furthermore, due to the localized nature of fatigue failure, even small variations in defect features can significantly affect the fatigue life of AM parts. While many studies on the effects of layer orientation and inter-layer time interval are available, a systematic investigation to evaluate the effects of geometry changes on the microstructure, defect features, and mechanical properties of AM parts is missing in the literature. Such studies are needed to better understand specimen property to part performance relationships, which ultimately supports standardization, qualification and certification of AM materials/parts. Thus, this study is designed to fill this gap by conducting an investigation into the effect of part geometry on the tensile and fatigue properties of LB-PBF 17-4 PH SS in relation to defect size and distribution.

In this study, 17-4 PH SS, a martensitic/austenitic precipitation-hardenable stainless steel is selected as the material of interest due to its weld-ability, which makes it suitable for the additive manufacturing processes [24]. Additionally, this grade of stainless steels possesses superior mechanical properties including high yield and ultimate tensile strengths, fracture toughness, and corrosion resistance at working temperatures below 300 °C [25,26], making it a desired material for aerospace, naval, marine, and nuclear applications. After the introduction, experimental procedures are presented, followed by the results obtained from different experiments. The experimental results are then discussed based on variations in thermal history experienced during manufacturing, estimated based on microstructural analysis. Finally, some conclusions drawn from this study are presented.

Table 1
Chemical composition of 17-4 PH SS powder provided by LPW Technology Inc.

Element	Fe	Cr	Ni	Mo	Mn	Si	N
Weight (%)	Balance	15.6	4.03	< 0.01	0.24	0.29	0.01
Element	O	P	C	S	Cu	Nb	
Weight (%)	0.05	0.004	0.01	0.003	3.89	0.33	

2. Experimental procedures

2.1. Material and specimens preparation

Argon atomized 17-4 PH SS powder from LPW Inc. with the chemical composition shown in Table 1 was used in this study. All parts were fabricated in vertical direction (i.e. perpendicular to the build plate) using EOS M290, an LB-PBF machine, under nitrogen environment. Three different groups of part geometries, including a dog-bone part with 7 mm diameter (i.e. representing the laboratory specimen or the witness coupon) and two types of square rods with 12 × 12 mm^2 and 25 × 25 mm^2 cross-section (i.e. representing parts) as shown in Fig. 1(a–c), respectively, were fabricated. These parts were designed to introduce variations in thermal history resulting from differences in part size and geometry. All parts were fabricated using default process parameters provided by EOS, as listed in Table 2. As can be seen from Fig. 1 for each part category, there were several parts on the build plate resulting in inter-layer time intervals of 59 s, 52 s, and 59 s for dog-bones, small blocks, and large blocks, respectively. Additionally, to conduct an accurate melt pool size analysis at the gage section of specimens, one set of parts including both the dog-bone and square rods was also manufactured up to the middle of the gage section (i.e. half-built specimens), following the exact same inter-layer time intervals of full builds.

To reduce the variability in the specimens, dog-bone parts as well as small and large square rods were machined into identically sized round specimens, based on the schematic shown in Fig. 2(a), with uniform gage section following ASTM Standard E606 [27] with the dimensions presented in Fig. 2(b). It should be noted that the required minimum gage diameter of 6.35 mm in ASTM Standard E606 was deviated in this study to ensure an adequate removal of the material at the gage section of dog-bone specimens during the machining process [9]. The 25 × 25 mm^2 square blocks (i.e. large blocks) were first cut in the longitudinal direction into four square rods with equal cross-section of approximately 12 × 12 mm^2. For simplicity purposes, the specimens machined from the dog-bone parts, square rods with 12 × 12 mm^2 cross-section, and square rods with 25 × 25 mm^2 cross-section will be referred to, respectively, as dog-bone, small block, and large block specimens throughout this manuscript.

Due to the existence of precipitation mechanisms in 17-4 PH SS, the applied heat treatment procedure can have a significant effect on the mechanical behavior [28]. In this study, all of the machined specimens were subjected to CA-H1025 heat treatment condition in which the specimens were first heat treated at 1922 °F for half an hour followed by air cooling (solution treatment). In addition, specimens were further aged at 1025 °F for four hours followed by air cooling. It was shown in a recent study [28] that CA-H1025 heat treatment could be very effective in homogenizing the microstructure of LB-PBF 17-4 PH SS specimens. All the heat treating steps were conducted in a batch furnace in the argon environment. Following the heat treatment, specimens were polished using different grit sand papers to remove machining marks and eliminate any effects of surface condition on the fatigue behavior.

2.2. Mechanical testing

Mechanical characterizations, including quasi-static tensile and uniaxial fatigue tests, were performed using a closed-loop servo

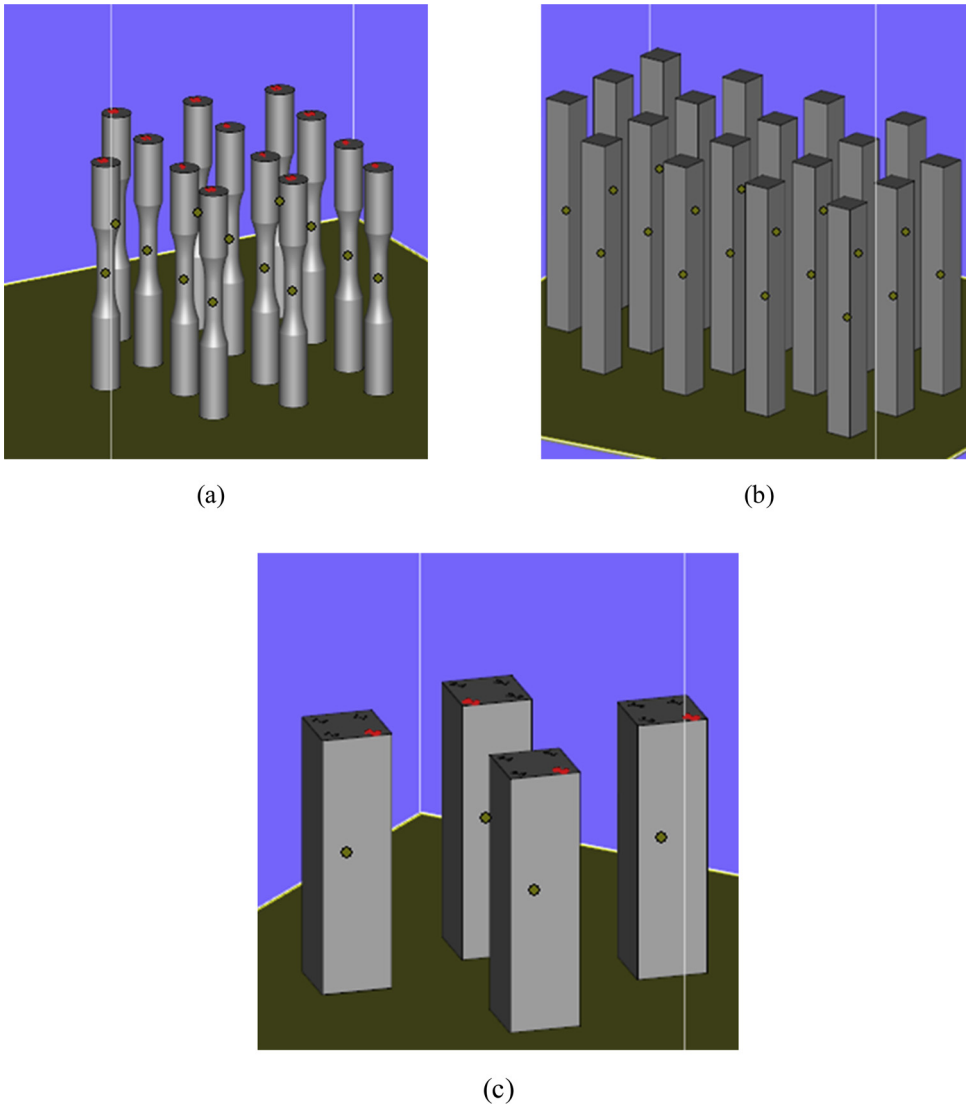

Fig. 1. LB-PBF 17-4 PH SS parts fabricated in vertical direction with three different geometries: (a) cylindrical dog-bone parts with 7 mm gage diameter, 90 mm height and a time interval of ~59 s, (b) small blocks with dimensions of 12 × 12 × 90 mm^3 and a time interval of ~52 s [33], and (c) large blocks with dimensions of 25 × 25 × 90 mm^3 with a time interval of ~59 s.

hydraulic MTS Landmark machine with load capacity of 100 kN. An MTS mechanical extensometer with a gage length of 10 mm was used to both measure the axial deformation on the gage section of the specimen as well as to control the test. As mentioned earlier, all of the specimens were fabricated following ASTM Standard E606 [27]; hence, the quasi-static tensile properties of LB-PBF 17-4 PH SS in this study were not obtained from specimens designed by following ASTM Standard E8/8 M [29] for tension testing. Quasi-static tensile tests were conducted at a strain rate of 0.001 s^{-1} first under strain-controlled mode up to 0.045 mm/mm strain followed by displacement-controlled mode until failure. Extensometer was removed after the strain-controlled mode portion of the test to prevent it from being damaged due to its small travel limit. Two tensile tests were conducted for each specimen type to confirm the consistency of the results.

Since the main purpose of this study was to investigate the effect of part geometry on the fatigue behavior and not to establish a strain-life curve for LB-PBF 17-4 PH SS, the uniaxial fatigue tests were conducted only at two fully-reversed (R_ε = -1) strain amplitudes of 0.0030 mm/mm and 0.0035 mm/mm. From the preliminary studies, LB-PBF 17-4 PH SS specimens subjected to CA-H1025 heat treatment procedure were seen to primarily exhibit elastic deformation at the strain amplitude of 0.0030 and 0.0035 mm/mm without any evidence of strain hardening or softening [28]. Hence, the fatigue tests in this study were first conducted under strain-controlled loading to determine the stable values of load and then switched to force-controlled mode until failure. The failure was defined as the complete separation of specimen. Each fatigue test for a specific part geometry was repeated three times at a particular strain level to verify the consistency of results.

Table 2
EOS recommended major process parameters utilized to fabricate LB-PBF 17-4 PH SS parts.

Laser power (W)	Scanning speed (mm/s)	Hatching space (μm)	Layer thickness (μm)	Layer rotation angle	Strip width (mm)
220	755.5	100	40	67°	100

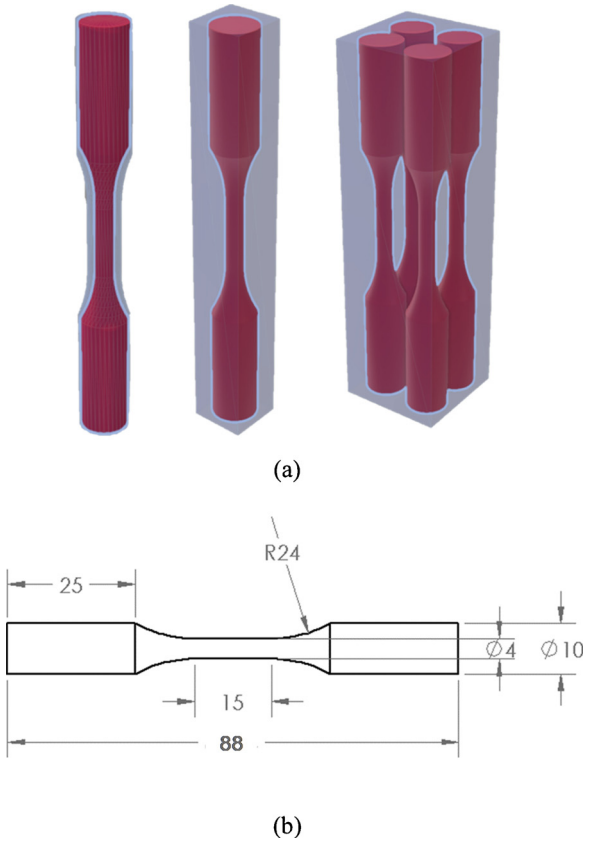

Fig. 2. (a) Schematics showing dog-bone parts, small blocks, and large blocks from which specimens were machined to the geometry and dimensions designed based on ASTM Standard E606 [27] and shown in (b). All dimensions are in mm.

2.3. Microstructure and fractography analysis

Two specimens, one without any heat treatment and one heat treated under CA-H1025 procedure, for each specimen type (i.e. dog-bone, small block, and large block) were cut at the middle of the gage section and then cold mounted in an epoxy resin solution to prepare optical micrograph samples following ASTM Standard E3-11 [30]. The samples were polished using different grit sand papers followed by colloidal silica suspension to obtain a mirror-like finish. The mirror finished samples were then used to quantify the defect size and distribution resulting from the variation in thermal history experienced by the fabricated parts. The distribution of porosity was determined from at least four different radial locations of the gage section and analyzed using an image processing software associated with the employed digital microscope. Only pores greater than 6 μm were considered in this study. Furthermore, the polished specimens were then etched using Beraha's tint etchant to conduct microstructural analysis to determine the effect of part size and geometry on the grain characteristics before and after heat treatment as well as to measure the melt pool size in non-heat treated specimens. To understand the factors responsible for crack initiation and failure in LB-PBF 17-4 PH SS specimens, fractography analysis was also performed on the failed fatigue specimens. Both optical microscopy and fractography analysis were conducted using a Keyence VHX-6000 digital microscope.

3. Experimental results

3.1. Microstructural analysis

Optical micrographs presenting the grain morphology for dog-bone, small block, and large block specimens in their longitudinal direction (i.e. perpendicular to the build plate) are shown in Fig. 3 in non-heat treated condition. During the additive manufacturing process, grains tend to grow in the opposite direction of heat transfer, which is from the solidifying melt pool to the previously solidified layers; therefore, elongated grains oriented perpendicular to the build plate (i.e. epitaxial

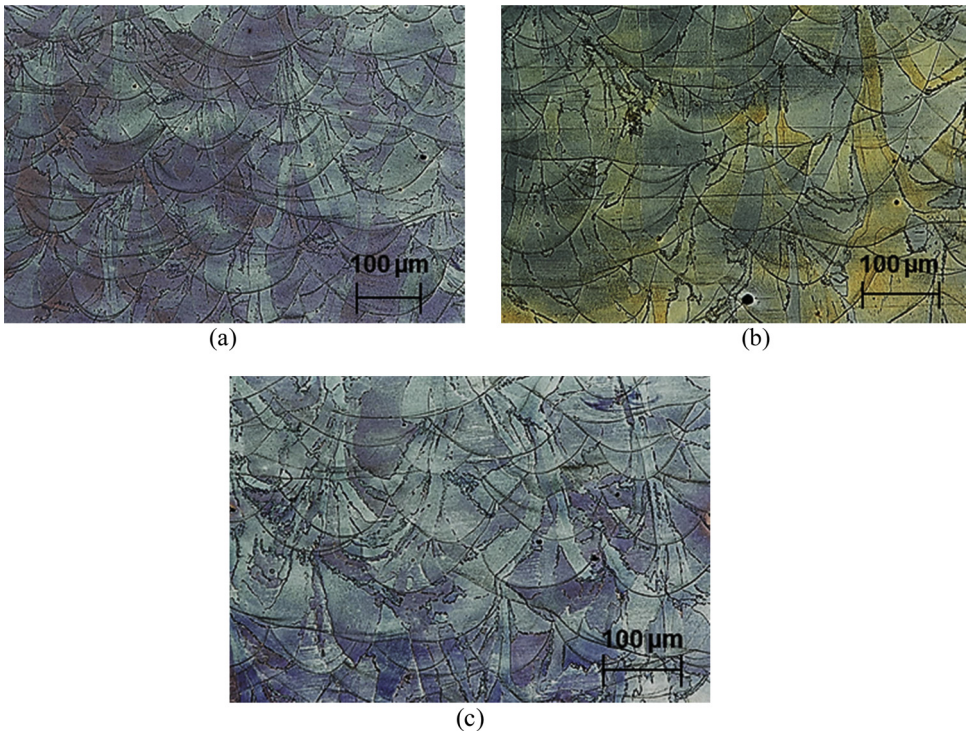

Fig. 3. Optical micrographs showing grain morphology in (a) dog-bone, (b) small block, and (c) large block specimens in their longitudinal direction (i.e. perpendicular to the build plate) in non-heat treated condition.

grain growth) are typically evident in AM parts [21,31]. Similar observation of elongated grains growing parallel to the build direction can be made for the non-heat treated LB-PBF 17-4 PH SS in Fig. 3.

Even though elongated grains were primarily seen in all of the specimen with different part geometries, some variation in the crystallographic texture was evident, which was revealed by the employed tint etchant. The orientation of epitaxial grains in the dog-bone specimens were observed to be mostly straight, while the grains in small and large block specimens were seen to be slightly oriented in different directions, (compare Fig. 3(a) with (b), and (c)). This type of variation in the orientation of epitaxial grain growth was also observed in [32], for LB-PBF 316 L SS, and reported to be affected by the size of the melt pool. The grains in smaller melt pools tend to grow straight from the bottom of the melt pool to the top, while grain growth was observed to be perpendicular to the melt pool boundary and oriented at different directions in larger melt pools [32]. The discrepancies in crystallographic texture in LB-PBF 17-4 PH SS specimens may also suggest the differences in the resulting melt pool size, which is affected by the variations in thermal history experienced during the fabrication of parts with different geometries. Furthermore, differences in thermal history can affect the pore size and distribution, and ultimately, the fatigue behavior of these parts.

Since all of the fatigue specimens were subjected to CA-H1025 heat treatment condition, microstructure characterizations were also conducted on the heat treated specimens in their longitudinal planes in Fig. 4 (a–c), respectively, for dog-bone, small block, and large block specimens. Significantly different microstructure features can be noticed between the heat treated and non-heat treated specimens by comparing Figs. 3 and 4. Primarily, elongated grains representing epitaxial growth as well as solidified melt pool lines were not visible in the heat treated specimens in Fig. 4. This can be attributed to the solution treatment (Condition A) conducted prior to the ageing process, which can homogenize the microstructure at a very high temperature of 1922 °F [28]. As a result, no distinct variation in the grain morphology among dog-bone, small block, and large block specimens are noticeable after CA-H1025 heat treatment in Fig. 4.

It should also be noted that the specimens were only subjected to a heat treatment procedure and no hot isostatic pressing (HIPing) was performed on them. Hence, the applied heat treatment should not have any considerable effects on the evolution of defects (i.e. entrapped gas pores and/or LoFs) in LB-PBF 17-4 PH SS specimens. Furthermore, conducting the heat treatment procedure eliminated the effect of microstructure by homogenization and most likely relieved any residual stresses resulting from the fabrication process, enabling this study to focus only on the effects of porosity, as they are affected by geometry, on the mechanical properties of LB-PBF 17-4 PH SS under monotonic tensile and fatigue loadings.

Porosity distribution at the gage section of dog-bone, small block, and large block specimens captured using the digital microscope along with their respective size distribution histogram are presented in Fig. 5(a–c), respectively. It should be again noted that statistics presented were collected from at least four different radial sections at the gage to be more representative of the porosity size distribution of these specimens and only pores greater than 6 μm in diameter were included in this analysis. Although a large number of pores can be seen in all of the specimens irrespective to the part geometry, a greater number of pores in the dog-bone specimen is noticeable from both optical micrograph and histogram presented in Fig. 5, when compared to the small and large block specimens.

As can be seen from Fig. 5, among the three groups of specimens, dog-bone specimens had slightly larger average pore size (11 μm), while the pore size was similar for small block (8 μm) and large block (8 μm) specimens. In addition, maximum defect size was also seen to be larger for the dog-bone specimen (˜31 μm) when compared to the small block (˜23 μm) and large block (˜22 μm) specimens. However, distinct variations in the number of defects greater than 6 μm in diameter were seen for specimens fabricated from different part geometries as dog-bone specimen had a larger number of pores (an average of 95 pores), followed by the small block specimen (an average of 55 pores), and large block specimen had the lowest number of defects (an average of 48 pores). Such variations in defect size and number can affect the mechanical properties of LB-PBF 17-4 PH SS, especially under fatigue loading. Although fatigue failure is a localized phenomenon, the presence of more defects, specifically if they are large and closer to the

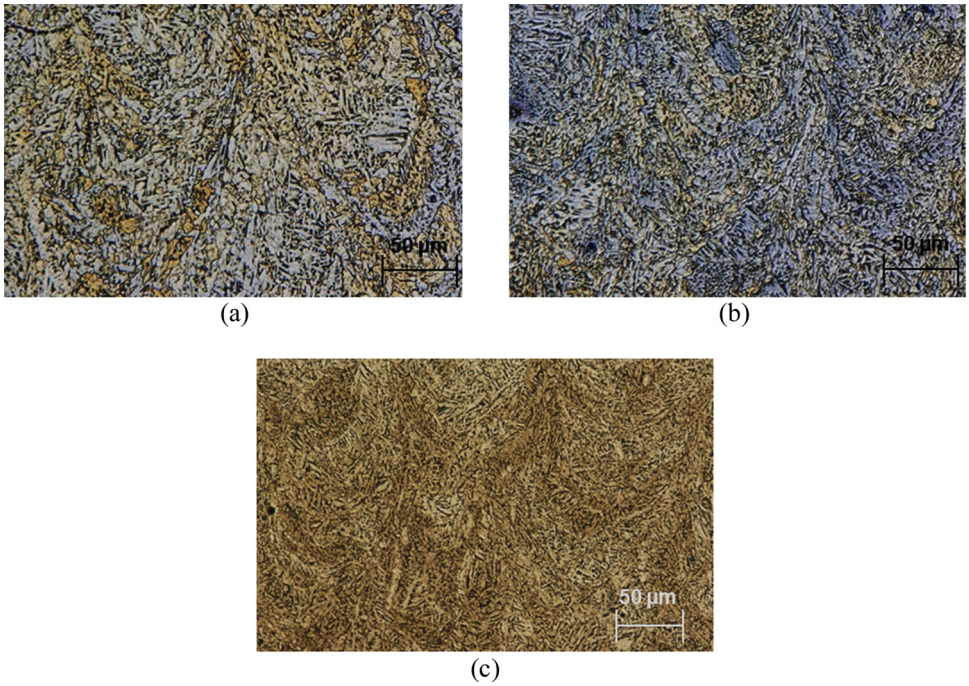

Fig. 4. Optical micrographs showing grain morphology in (a) dog-bone, (b) small block, and (c) large block specimens in their longitudinal direction (i.e. perpendicular to the build plate) and subjected to CA-H1025 heat treatment.

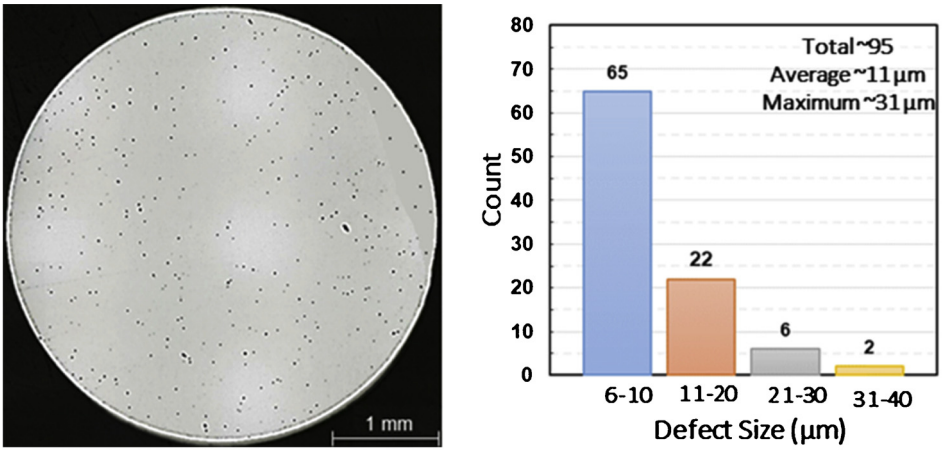

(a)

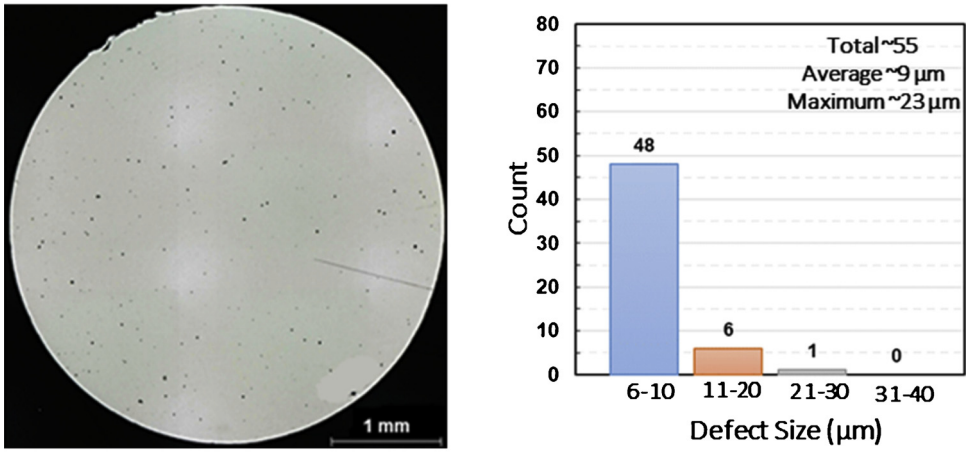

(b)

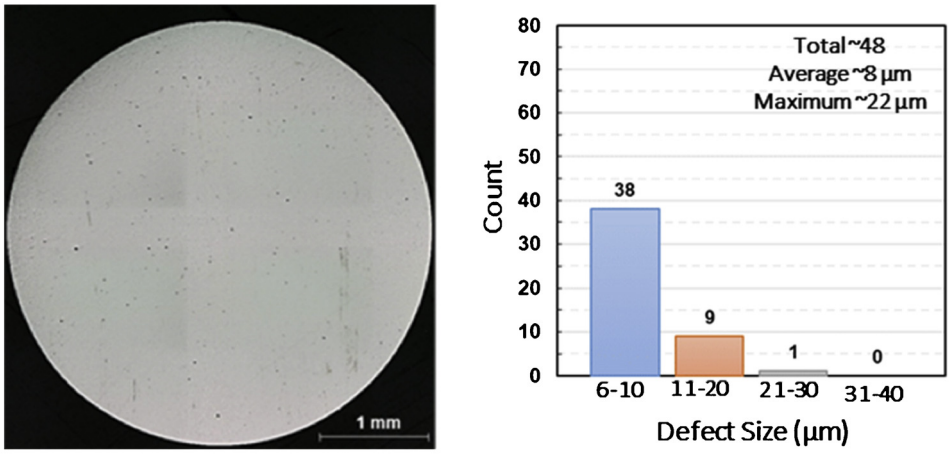

(c)

Fig. 5. Optical micrographs showing the porosity size distribution along with their respective histogram in the gage section of (a) dog-bone, (b) small block, and (c) large block specimens.

surface, can increase the probability of crack initiation at less number of cycles, which ultimately reduces the fatigue strength.

It should be mentioned here again that the sizes and numbers reported in Fig. 5 are from 2D analysis of 4 cross-sectional areas per specimen. While the information collected can be helpful in explaining some of the mechanical behaviors observed, a 3D analysis of defects within the entire gage section may be needed to capture the true effect of geometry on the defect size distribution. For example, the large block specimen is expected to have smaller size defects as compared to the small block specimen; however, the maximum defect captured from the

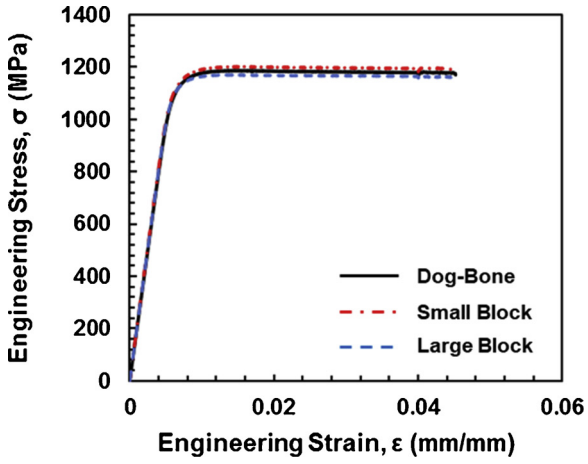

Fig. 6. Monotonic tensile behavior of CA-H1025 17-4 PH SS specimens machined from parts with different geometries and presented by (a) engineering stress versus engineering strain curves prior to the removal of the extensometer, and (b) engineering stress versus displacement curves up to failure.

Table 3
Monotonic tensile properties of LB-PBF 17-4 PH SS specimens machined from parts with different geometries along with the wrought counterpart reported in [34].

Properties	Dog-Bone	Small Block	Large Block	Wrought
σ_y (MPa)	1180 ± 20	1198 ± 27	1145 ± 5	1000
σ_u (MPa)	1195 ± 6.5	1231 ± 28	1171 ± 0.25	1070
ε_f (mm/mm)	0.33 ± 0.01	0.33 ± 0.02	0.37 ± 0.01	N/A

2D analysis of 4 cross-sectional areas were almost similar, 22 μm for the large block specimen and 23 μm for the small block specimen. The number of defects for each specimen is expected to be the most accurate information gained from the 2D analysis.

3.2. Monotonic tensile behavior

Engineering stress versus engineering strain curves obtained from monotonic tensile tests prior to the removal of the extensometer and engineering stress versus displacement curves up to failure for dog-bone, small block, and large block specimens are presented in Fig. 6(a) and (b), respectively. Furthermore, the average along with upper and lower values of tensile properties, including yield strength, σ_y, ultimate tensile strength, σ_u, and fracture strain, ε_f, obtained from two repeated tests for each specimen type along with those reported for the wrought counterpart under the same heat treatment are listed in Table 3 [33,34]. Although all three specimen types exhibited varying amount of porosity as seen from the optical micrographs in Fig. 5, such variations did not have much effects on the tensile properties. Having similar tensile properties may also suggest that the final microstructure of dog-bone, small block, and large block specimens were similar as a result of the applied CA-H1025 heat treatment.

Higher values of yield and ultimate tensile strengths for LB-PBF 17-4 PH SS as compared to the ones for the wrought counterpart and subjected to the identical heat treatment procedure (i.e. CA-H1025) are noticeable from Table 3. Better tensile properties of AM materials as compared to their wrought counterparts have been also reported in other studies [35–37] and attributed to the finer grains resulting from the higher cooling rate inherent to the laser-based additive manufacturing processes. It may be worth reminding that all of the tensile tests in this study were conducted on the specimens designed following the ASTM Standard E606 for strain-controlled fatigue testing [27] and

Table 4
Uniaxial strain-controlled fatigue test results for LB-PBF 17-4 PH SS specimens machined from parts with different geometries.

Specimen I.D	ε_α (mm/mm)	σ_α (MPa)	σ_m (MPa)	$2N_f$ (Reversals)
		Dog − Bone		
S02	0.0030	597	−11	145,330
S04		601	1	203,326
S03		598	5	267,225
S05	0.0035	697	18	67,402
S06		703	−3	89,462
S07		708	20	108,246
		Small Block		
S02	0.0030	622	5	317,060
S03		609	−11	434,606
S01		641	16	1,173,562
S06	0.0035	710	−2	122,300
S04		720	−20	123,384
S05		710	20	128,870
		Large Block		
S07	0.0030	612	3	291,130
S02		610	4	852,858
S03		610	4	4,165,068
S06	0.0035	712	−20	35,132
S05		721	0	107,886
S04		718	2	117,520

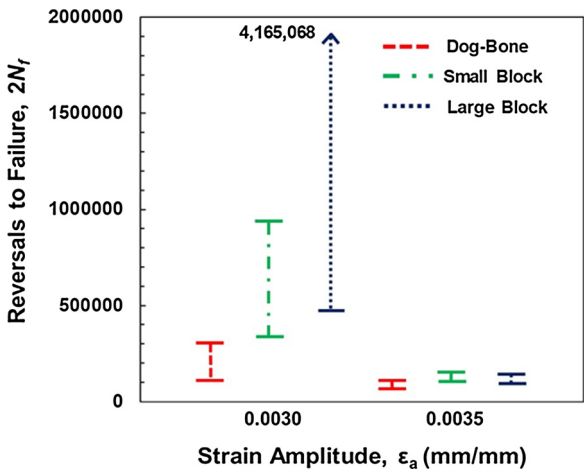

Fig. 7. The chart showing the variation in fatigue lives along with upper and lower values obtained for dog-bone, small block, and large block specimens under uniaxial fully-reversed strain-controlled fatigue loading at strain amplitudes of 0.0030 and 0.0035 mm/mm.

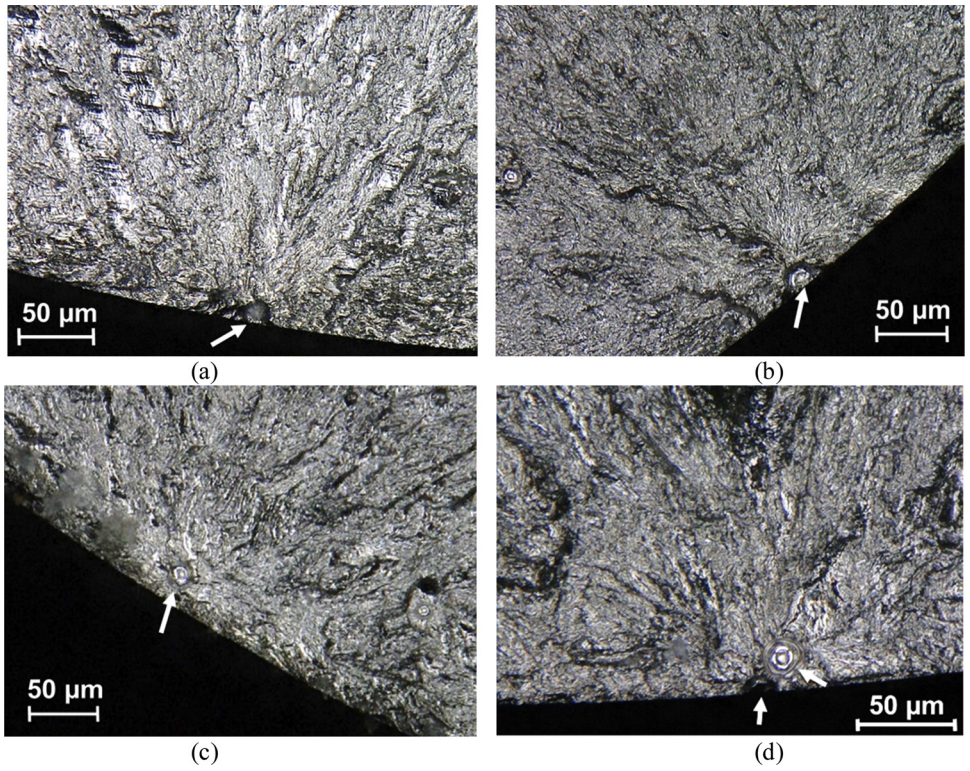

Fig. 8. Fracture surfaces showing pores responsible for the crack initiation and failure in (a) a dog-bone specimen ($2N_f$ = 267,226 reversals), (b) a small block specimen ($2N_f$ = 1,173,562 reversals), and (c) a large block specimen ($2N_f$ = 4,165,068 reversals). (d) Fracture surface of a dog-bone specimen with two pores within a close proximity with each other and responsible for crack initiation and failure. All specimens were subjected to 0.0030 mm/mm strain amplitude.

not the ASTM Standard E8 for tension testing [29]. This deviation should mostly affect the measured fracture strains and not the yield and ultimate tensile strength values.

3.3. Fatigue behavior and fractography analysis

Due to the localized nature of fatigue failure, the presence of defects, such as pores and LoFs, can have a detrimental effect on the structural integrity of AM parts under cyclic loading as these defects affect the localized stress field and cause stress concentration. Accordingly, any variations in defects' size, location, and shape (see Fig. 5) are expected to cause variations in the fatigue strength of LB-PBF 17-4 PH SS. Fatigue test results are listed in Table 4 and line chart presenting the variation in fatigue lives along with upper and lower values obtained from at least three repeated tests at two different strain amplitudes of 0.0030 and 0.0035 mm/mm for dog-bone, small block, and large block specimens are shown in Fig. 7. As it can be seen from this figure, part geometry has a significant effect on the fatigue behavior of LB-PBF 17-4 PH SS specimens at high cycle regime (i.e. at lower strain amplitude of 0.0030 mm/mm) as large block specimens exhibited the longest fatigue lives, followed by small block specimens, while dog-bone specimens had the shortest fatigue lives.

The fatigue life results presented in Fig. 7 can be explained to some extend based on the variations in the defect size and number shown in Fig. 5. The large block specimens, which exhibited the longest fatigue strength had the lowest amount of porosity as well as smaller average pore size of 8 μm, while the dog-bone specimens with the highest amount of porosity and an average pore size of 11 μm had the shortest fatigue lives. Furthermore, such variations in the fatigue strength were primarily seen in the high cycle regime (i.e. the lower strain amplitude of 0.0030 mm/mm), where the effect of defects are more significant compared to the low cycle fatigue regime (i.e. the higher strain amplitude of 0.0035 mm/mm). It is well established that defects have a more significant effect in the high cycle fatigue regime where the deformation is mostly elastic and defects generate higher stress concentrations [38].

To further understand the factors responsible for crack initiation and failure in the LB-PBF 17-4 PH SS specimens, fractography analysis was performed on the failed specimens. Example fracture surfaces of dog-bone, small block, and large block specimens, all of which were subjected to a strain amplitude of 0.0030 mm/mm, are shown in Fig. 8(a–c), respectively. In all of these specimens, cracks were observed to initiate from pores located at or near the surface as indicated by the white arrows in Fig. 8. Upon further analysis, the size of the pores was found to be the main factor influencing the resulting fatigue life of the specimen, while there was not much variation in the location of the crack initiating pores.

In Fig. 8, the longest fatigue life was achieved for the large block specimen ($2N_f$ = 4,165,068 reversals) with smallest pore size of ~14 μm, followed by the small block specimen ($2N_f$ = 1,173,562 reversals) with a pore size of ~20 μm, and the shortest fatigue life was obtained for the dog-bone specimen ($2N_f$ = 267,226 reversals) with the largest pore size of ~26 μm. Furthermore, in the case of a few dog-bone specimens, cracks were observed to initiate from two adjacent pores both located close to the surface, such as the one represented by white arrows in Fig. 8(d). It is also worth mentioning that higher amount of porosity was noticed in dog-bone specimens in Fig. 5, which may suggests a higher probability of cracks to initiate from multiple pores in a close proximity of each other.

From the fractography analysis conducted on all of the specimens subjected to fatigue loading, the average pore size responsible for crack initiation and failure was calculated for each specimen type subjected to strain amplitude of 0.0030 mm/mm. The average pore size was found to be larger for dog-bone specimens (~29 μm), which also exhibited the shortest fatigue lives. On the other hand, the average pore size was measured to be (~20 μm) for small block specimen, while it was smallest (~17 μm) for large block specimens, which also exhibited the highest fatigue strength. Therefore, optical micrographs and fractography analysis results may suggest that the fatigue strength of LB-PBF 17-4 PH SS specimens, at least at high cycle regime, is primarily governed by the distribution and size of pores in the specimen, which can be affected by the thermal history experienced during the fabrication

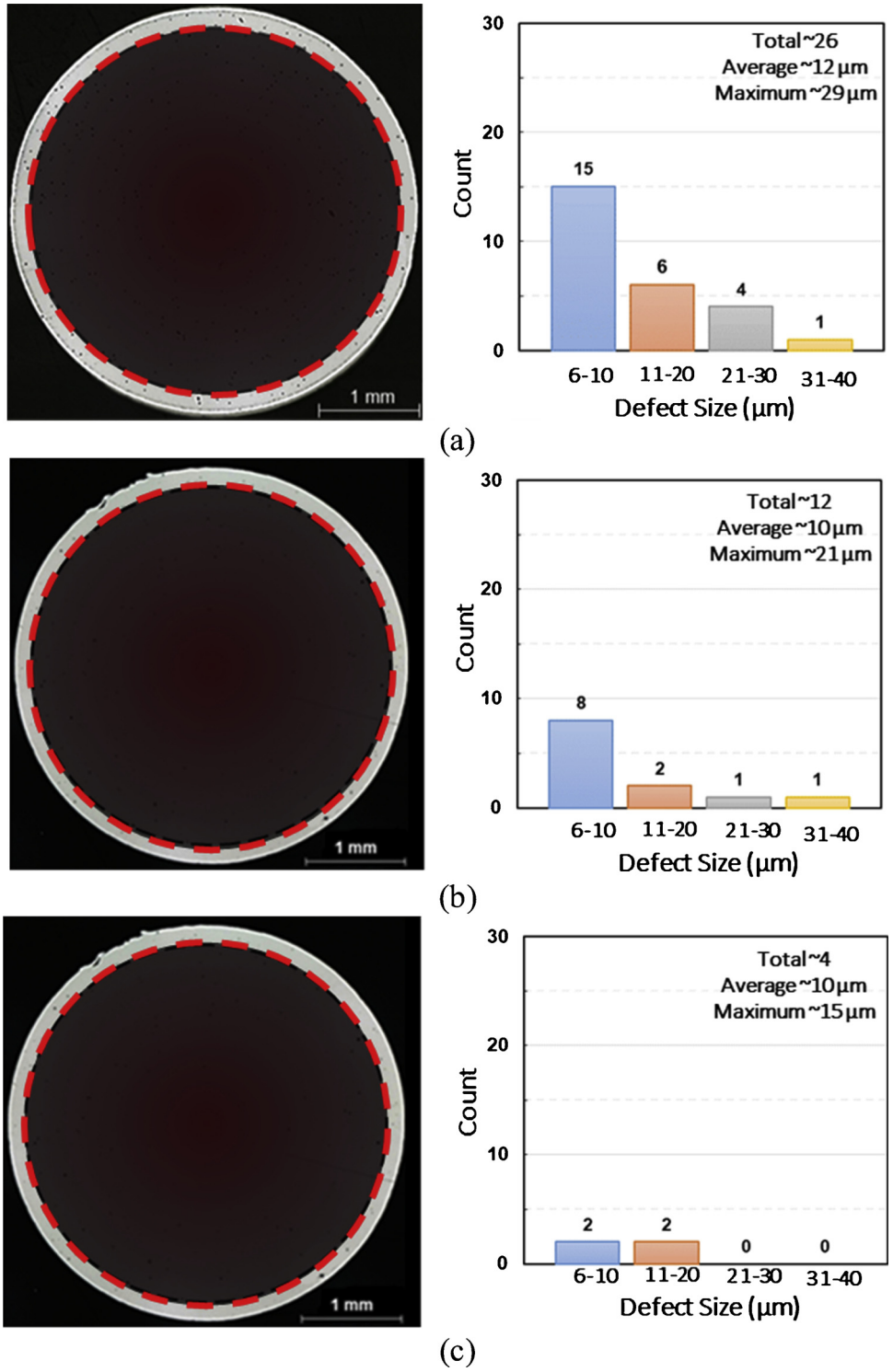

Fig. 9. Optical micrographs showing the porosity within the 100 µm from the surface (i.e. pores in the highlighted region are excluded from the analysis) along with their size distributions for (a) dog-bone, (b) small block, and (c) large block specimens.

process.

4. Discussion on experiential observations

As seen in Fig. 5, although similar size pores were seen in the large and small block specimens, the large block specimens still exhibited better fatigue resistance in Fig. 7. From the fractography analysis in Fig. 8, the entrapped gas pores responsible for the crack initiation and failure in LB-PBF 17-4 PH SS were all seen to be located close to the surface and within 100 µm of it. Hence, a defect size distribution analysis was conducted to determine the number and size of pores located within the 100 µm from the surface and the results are presented in Fig. 9(a–c), respectively, for dog-bone, small block, and large block specimens.

Among three types of specimens utilized in this study, large block specimens contained the lowest number of pores (˜4) along with the smallest maximum pore size of ˜15 µm, followed by small block specimens with ˜12 pores and a maximum pore size of ˜21 µm, while dog-

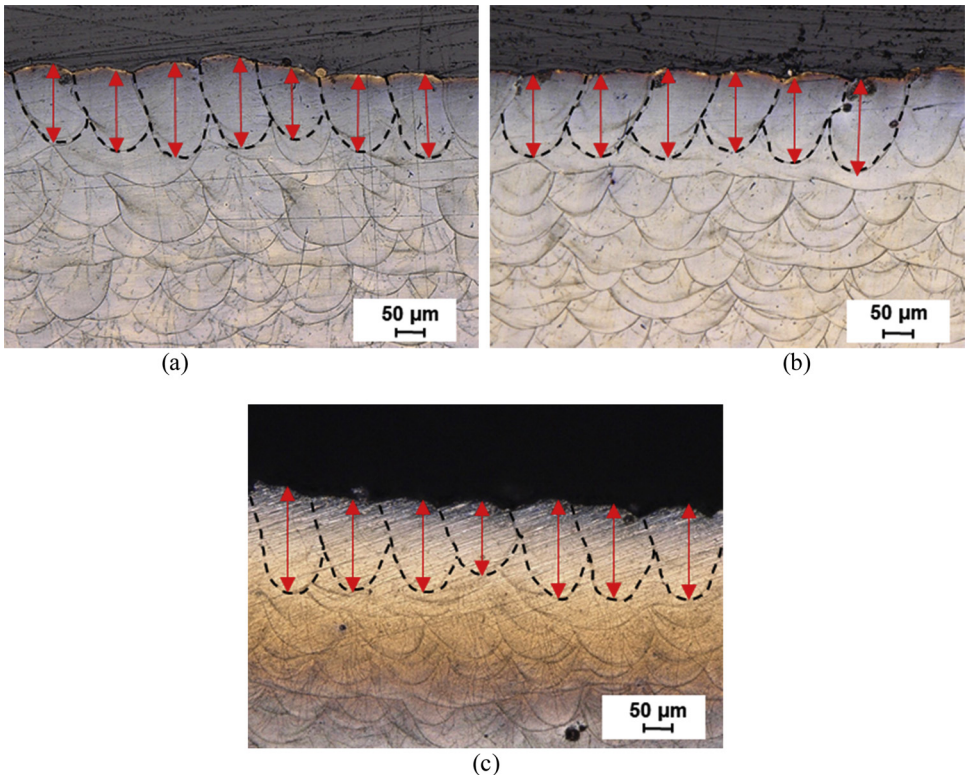

Fig. 10. Optical micrographs showing variation in melt pool depth at the very top layer of a half-built (a) a dog-bone specimen with 142 µm average melt pool depth, (b) a small block specimen with 156 µm average melt pool depth, and (c) a large block specimen with 162 µm average melt pool depth in their transverse direction (i.e. perpendicular to the build plate) in non-heat treated condition.

bone specimens had both the highest number of pores (˜27) as well as the largest maximum pore size of ˜29 µm, all within 100 µm from the specimen surface. Hence, due to the fact that the surface defects are more detrimental than the defects located away from the surface [38], large block specimens exhibited better fatigue resistance as compared to the small block and dog-bone specimens.

Figs. 5,7, and 9 highlighted significant variations in porosity and fatigue strength of specimens machined from LB-PBF 17-4 PH SS parts with deferent sizes and geometries. It is hypothesized that such variations are coming from the differences in thermal history experienced during additive manufacturing process as a result of changes in part geometry and size. The localized thermal history experienced by the part can significantly influence resulting melt pool characteristics [39]. Therefore, to further investigate the effect of part geometry and size on the thermal history, microstructural analyses were conducted to characterize the melt pool dimensions on non-heat treated specimens from three different geometries utilized in this study; dog-bone, small block, and large block. Non-heat treated specimens were chosen for this analysis as the melt pools would not be distinguishable after conducting CA-H1025 heat treatment.

It is also worth noting that due to the small layer thickness of 40 µm for 17-4 PH SS, the melt pool created in one layer can influence the melt pools created in the previously solidified layer(s); this is because the process parameters are typically selected to ensure that the melt pool depth is larger than the layer thickness to avoid LoF defects. On the other hand, the laser beam used as the heat source also rotates by 67° in every layer, which results in the rotation of the melt pool tracks. To better measure the melt pool size at the gage section of specimens, similar geometries as the ones used in Fig. 1 with the exact inter-layer time intervals were fabricated up to the middle of the gage section. Basically, the fabrication was stopped half way for three reasons. First, the melt pools at the top of these parts were not influenced by subsequent layers. Second, the exact direction of the laser beam could be easily seen at the top layer, enabling a more accurate calculation of melt pool dimensions. Third, the melt pools at the top layers were representatives of the melt pools at the gage section of dog-bone, small block, and large block specimens. This process of determining the melt pool dimensions at the top layer is also suggested in [40].

The melt pools observed at the middle of the top layer (i.e. very last layer) of half-built dog-bone, small block, and large block parts are presented in Fig. 10(a–c), respectively. ImageJ software was used to calculate the melt pool dimensions including depth of melt pool, d_p, and the depth of overlap between the consecutive melt pools, d_o [40] for all the micrographs presented in Fig. 10. A larger average melt pool depth of ˜162 µm was measured in large block specimens, while shorter average melt pool depths of ˜156 µm and ˜142 µm were obtained for small block and dog-bone specimens, respectively. The differences seen in the melt pool size of different specimens imply that dog-bone, small block, and large block parts have experienced some variations in thermal history, which can in turn explain the variations observed in their porosity levels and fatigue behaviors. The ratios of melt pool depth, d_p, to layer thickness, t_L, and depth of overlap between consecutive melt pools, d_o, to layer thickness, t_L, were also determined (see Fig. 3 of NASA document [40]). For all of the specimens, irrespective to part geometry, the values of d_o/t_L and d_p/t_L were calculated to be greater than one. The deeper melt pool than the layer thickness as well as adequate overlap between the consecutive melt pools in all specimen types can explain not seeing LoF defects in these specimens.

To further understand the variation in the porosity seen within close proximity of the surface of dog-bone, small block, and large block specimens in Fig. 9, melt pool analysis was also conducted at the region from which the specimens were machined. The analysis was focused at the section closest to the surface of the specimens as shown in Fig. 11 (a–c) for dog-bone, small block, and large block specimens, respectively. Similarly, a shallower average melt pool depth of ˜136 µm was measured for the dog-bone specimen, followed by ˜148 µm for the small block specimen, while the deepest average melt pool of ˜158 µm was observed for the large block specimen.

Shorter melt pool depths and more vertically oriented grain growth observed in dog-bone specimens can be associated with the lower temperature of the solidified material upon which a new layer is fabricated, resulting in a higher cooling rate [32] experienced by these

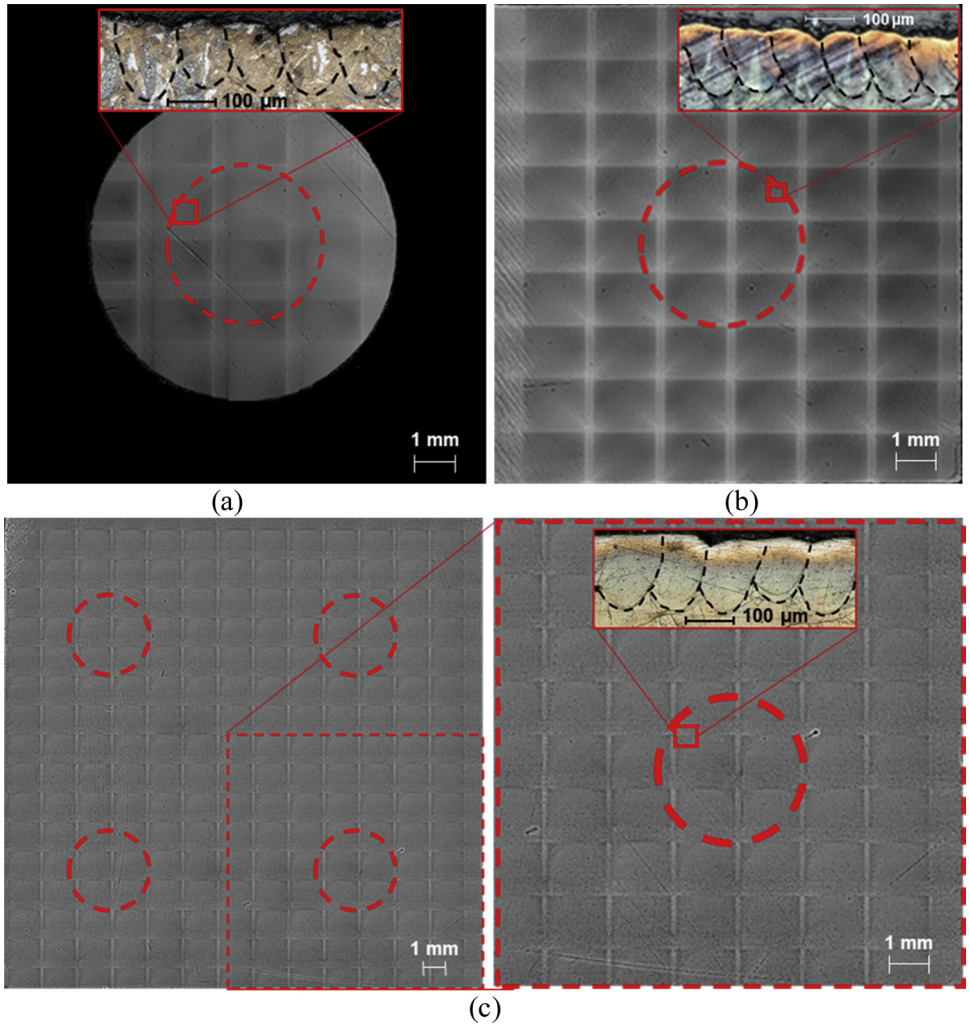

Fig. 11. Optical micrographs showing variations in melt pool depth at the region where the fatigue specimens were machined in (a) a dog-bone specimen with 136 µm average melt pool depth, (b) a small block specimen with 148 µm average melt pool depth, and (c) a large block specimen with 158 µm average melt pool depth.

specimens as compared to the small and large block specimens. On the other hand, the larger melt pool size of large block specimens is an indication of a lower cooling rate experienced by these specimens during fabrication, which is most likely derived by the higher temperature of the solidified material upon which a new layer is fabricated. The higher cooling rate, and consequently, the faster solidification in dog-bone specimens decreases the time for the gas pores to escape the melt pool and results in them transforming into entrapped gas pores [41]. This explains the more and larger pores in dog-bone specimens as well as less and smaller pores in large block specimens, as evident in Figs. 5 and 9. Similarly, Liu et al. [42] reported the presence of entrapped gas pores resulting from the evaporation of tin in the struts of Ti-24Nb-4Zr-8Sn porous structures. Larger entrapped gas pores were seen for the parts fabricated using selective laser melting process as compared to the ones fabricated using electron beam melting process, which was attributed to the higher cooling rate associated with the selective laser melting process.

In summary, this study suggests that a good understanding of the effects of part geometry and size on the resulting thermal history, which can significantly affect the distribution of porosity, and consequently, the fatigue lives of AM parts is necessary to successfully establish specimen property to part performance relationships. Similarity in thermal histories between test specimens and the critical location of the part, by altering process parameters, may be the key for establishing property-performance relationships of AM parts.

5. Conclusions

In the current study, the effect of part size and geometry on the melt pool dimensions and porosity distribution and how they influence the tensile and fatigue behavior of 17-4 PH stainless steel (SS) fabricated using a laser beam powder bed fusion (LB-PBF) process were investigated. The variation in the fatigue lives of specimens were related to the size and number of entrapped gas pores acting as the crack initiation sites. Since the formation and distribution of these defects are primarily affected by the thermal history experienced during the laser based fabrication, microstructural analysis was performed to determine variations in melt pool size as an indicator of the experienced thermal history during additive manufacturing. Based on the experimental results and discussions presented, the following conclusions can be drawn:

1 Optical micrographs showed a higher amount of porosity as well as larger pores in the dog-bone specimen as compared to the ones in small and large block specimens.
2 Irrespective to the variations observed in the amount of porosity among specimens machined from parts with different sizes and geometries, the effect of geometry on the tensile properties of LB-

PBF 17-4 PH SS was minimal. The values of yield and ultimate tensile strengths ranged between 1145 to 1198 MPa and 1171 to 1231 MPa, respectively. Similarity in the tensile properties may have been resulting from the homogenization of microstructure after CA-H1025 heat treatment.

3 The large block specimens with not only less, but also smaller pores within a close proximity of the surface, exhibited the highest fatigue strength, followed by small block specimens, while the dog-bone specimens with largest pores had the shortest fatigue lives.

4 From the fractography analysis, the pores responsible for crack initiation were larger for dog-bone specimens when compared to the ones for large and small block specimens. In some cases, cracks were found to initiate from two pores located in a close proximity with one another in the dog-bone specimens, which had a higher number of pores and shorter fatigue lives.

5 Microstructural analysis revealed a smaller average melt pool depth for dog-bone specimens, while it was the deepest in the large block specimens. The shorter melt pool depth in dog-bone specimens can be associated to the higher temperature gradient and cooling rate resulting in less time for the gas bubbles to escape, which can lead to formation of not only larger, but also a higher number of entrapped gas pores.

This study showed that a small change in size and/or geometry of the part fabricated using LB-PBF can significantly affect the formation and distribution of defects, which ultimately govern the structural integrity of the part under cyclic loading. This raises an important issue on how to relate and use the properties obtained from small laboratory specimens or witness coupons to evaluate the part performance in fatigue critical applications. Therefore, further studies need to be conducted to better understand property-performance relationships as they are affected by process-structure relationships and develop a procedure on how to design specimens to be representative of the critical location of the part under service loading. Such studies are indeed necessary in enabling standardization, qualification, and certification of AM parts in safety critical applications.

Declaration of Competing Interest

None

Acknowledgement

This paper is based upon the work partially supported by the ASTM International Additive Manufacturing Center of Excellence (AM CoE) and U.S. Naval Air Systems Command (NAVAIR).

References

[1] S. Romano, L. Patriarca, S. Foletti, S. Beretta, LCF behaviour and a comprehensive life prediction model for AlSi10Mg obtained by SLM, Int. J. Fatigue 117 (2018) 47–62.
[2] S.M.J. Razavi, P. Ferro, F. Berto, Fatigue assessment of Ti–6Al–4V circular notched specimens produced by selective laser melting, Metals 7 (2017) 291.
[3] S.R. Daniewicz, N. Shamsaei, An introduction to the fatigue and fracture behavior of additive manufactured parts, Int. J. Fatigue 94 (2017) 167.
[4] A.J. Sterling, B. Torries, N. Shamsaei, S.M. Thompson, D.W. Seely, Fatigue behavior and failure mechanisms of direct laser deposited Ti–6Al–4V, Mater. Sci. Eng. A 655 (2016) 100–112.
[5] R. Molaei, A. Fatemi, Fatigue design with additive manufactured metals: issues to consider and perspective for future research, Procedia Eng. 213 (2018) 5–16.
[6] W.E. Frazier, Metal additive manufacturing: a review, J. Mater. Eng. Perform. 23 (2014) 1917–1928.
[7] A. Yadollahi, N. Shamsaei, S.M. Thompson, D.W. Seely, Effects of process time interval and heat treatment on the mechanical and microstructural properties of direct laser deposited 316L stainless steel, Mater. Sci. Eng. A 644 (2015) 171–183.
[8] M. Seifi, M. Gorelik, J. Waller, N. Hrabe, N. Shamsaei, S. Daniewicz, J.J. Lewandowski, Progress towards metal additive manufacturing standardization to support qualification and certification, J. Min. Metals Mat. Soc. 69 (2017) 439–455.
[9] A. Yadollahi, N. Shamsaei, Additive manufacturing of fatigue resistant materials: challenges and opportunities, Int. J. Fatigue 98 (2017) 14–31.
[10] M. Seifi, A. Salem, D. Satko, J. Shaffer, J.J. Lewandowski, Defect distribution and microstructure heterogeneity effects on fracture resistance and fatigue behavior of EBM Ti–6Al–4V, Int. J. Fatigue 94 (2017) 263–287.
[11] R. Cunningham, S.P. Narra, C. Montgomery, J. Beuth, A.D. Rollett, Synchrotron-Based X-ray Microtomography Characterization of the Effect of Processing Variables on Porosity Formation in Laser Power-Bed Additive Manufacturing of Ti-6Al-4V, JOM 69 (2017) 479–484.
[12] C. Weingarten, D. Buchbinder, N. Pirch, W. Meiners, K. Wissenbach, R. Poprawe, Formation and reduction of hydrogen porosity during selective laser melting of AlSi10Mg, J. Mater. Process. Technol. 221 (2015) 112–120.
[13] L. Sheridan, O.E. Scott-Emuakpor, T. George, J.E. Gockel, Relating porosity to fatigue failure in additively manufactured alloy 718, Mater. Sci. Eng. A 727 (2018) 170–176.
[14] M. Simonelli, Y.Y. Tse, C. Tuck, Effect of the build orientation on the mechanical properties and fracture modes of SLM Ti–6Al–4V, Mater. Sci. Eng. A 616 (2014) 1–11.
[15] P. Edwards, M. Ramulu, Fatigue performance evaluation of selective laser melted Ti–6Al–4V, Mater. Sci. Eng. A 598 (2014) 327–337.
[16] A. Yadollahi, N. Shamsaei, S.M. Thompson, A. Elwany, L. Bian, Effects of building orientation and heat treatment on fatigue behavior of selective laser melted 17-4 PH stainless steel, Int. J. Fatigue 94 (2017) 218–235.
[17] R. Shrestha, J. Simsiriwong, N. Shamsaei, Fatigue behavior of additive manufactured 316L stainless steel parts: effects of layer orientation and surface roughness, Addit. Manuf. 28 (2019) 23–38.
[18] B. Torries, N. Shamsaei, Fatigue behavior and modeling of additively manufactured Ti-6Al-4V including interlayer time interval effects, J. Min. Metals Mat. Soc. 69 (2017) 2698–2705.
[19] J. Zhao, M. Easton, M. Qian, M. Leary, M. Brandt, Effect of building direction on porosity and fatigue life of selective laser melted AlSi12Mg alloy, Mater. Sci. Eng. A 729 (2018) 76–85.
[20] A. Fatemi, R. Molaei, J. Simsiriwong, N. Sanaei, J. Pegues, B. Torries, N. Phan, N. Shamsaei, Fatigue behaviour of additive manufactured materials: an overview of some recent experimental studies on Ti-6Al-4V considering various processing and loading direction effects, Fatigue Fract. Eng. Mater. Struct. 42 (2019) 991–1009.
[21] J. Pegues, M. Roach, R.S. Williamson, N. Shamsaei, Surface roughness effects on the fatigue strength of additively manufactured Ti-6Al-4V, Int. J. Fatigue 116 (2018) 543–552.
[22] M. Mahmoudi, A. Elwany, A. Yadollahi, S.M. Thompson, L. Bian, N. Shamsaei, Mechanical properties and microstructural characterization of selective laser melted 17-4 PH stainless steel, Rapid Prototyp. J. 23 (2017) 280–294.
[23] K.V. Yang, P. Rometsch, T. Jarvis, J. Rao, S. Cao, C. Davies, X. Wu, Porosity formation mechanisms and fatigue response in Al-Si-Mg alloys made by selective laser melting, Mater. Sci. Eng. A 712 (2018) 166–174.
[24] J. Hunt, F. Derguti, I. Todd, Selection of steels suitable for additive layer manufacturing, Ironmak. Steelmak. 41 (2014) 254–256.
[25] C. Schade, Processing, Microstructures and Properties of a Dual Phase Precipitation-hardening PM Stainless Steel, PhD Thesis, Drexel University, 2010.
[26] X. Lin, Y. Cao, X. Wu, H. Yang, J. Chen, W. Huang, Microstructure and mechanical properties of laser forming repaired 17-4PH stainless steel, Mater. Sci. Eng. A 553 (2012) 80–88.
[27] ASTM E606-04, Standard Practice for Strain-Controlled Fatigue Testing, ASTM International, West Conshohocken, PA, 2004.
[28] P.D. Nezhadfar, R. Shrestha, N. Phan, N. Shamsaei, Fatigue behavior of additively manufactured 17-4 PH stainless steel: synergistic effects of surface roughness and heat treatment, Int. J. Fatigue 124 (2019) 188–204.
[29] ASTM E8/8M-16a, Standard Test Methods for Tension Testing of Metallic Materials, ASTM International, West Conshohocken, PA, 2016.
[30] ASTM E3-11, Standard Guide for Preparation of Metallographic Specimens, ASTM International, West Conshohocken, PA, 2017.
[31] M. Masoomi, S.M. Thompson, N. Shamsaei, Laser powder bed fusion of Ti-6Al-4V parts: thermal modeling and mechanical implications, Int. J. Mach. Tools Manuf. 118 (2017) 73–90.
[32] Z. Sun, X. Tan, S.B. Tor, C.K. Chua, Simultaneously enhanced strength and ductility for 3D-printed stainless steel 316L by selective laser melting, NPG Asia Mater. 10 (2018) 127–136.
[33] R. Shrestha, P.D. Nezhadfar, M. Masoomi, J. Simsiriwong, N. Phan, N. Shamsaei, Effects of design parameters on thermal history and mechanical behavior of additively manufactured 17-4 PH stainless steel, Proceedings of the 29th Annual International Solid Freeform Symposium - An Additive Manufacturing Conference, (2018), pp. 1277–1289.
[34] ASTM A693-16, Standard Specification for Precipitation-hardening Stainless and Heat Resisting Steel Plate, Sheet, and Strip, ASTM International, West Conshohocken, PA, 2016.
[35] A.B. Spierings, T.L. Starr, K. Wegener, Fatigue performance of additive manufactured metallic parts, Rapid Prototyp. J. 19 (2013) 88–94.
[36] N. Shamsaei, A. Yadollahi, L. Bian, S.M. Thompson, An overview of Direct Laser Deposition for additive manufacturing; Part II: mechanical behavior, process parameter optimization and control, Addit. Manuf. 8 (2015) 12–35.
[37] Y.J. Liu, Y.S. Zhang, L.C. Zhang, Transformation-induced plasticity and high strength in beta titanium alloy manufactured by selective laser melting, Materialia 6 (2019) 100299.
[38] R.I. Stephens, A. Fatemi, R.R. Stephens, H.O. Fuchs, Metal Fatigue in Engineering, John Wiley & Sons, 2000.
[39] T.G. Spears, S.A. Gold, In-process sensing in selective laser melting (SLM) additive manufacturing, Integr. Mater. Manuf. Innov. 5 (2016), https://doi.org/10.1186/

s40192-016-0045-4.
[40] Specification for Control and Qualification of Laser Powder Bed Fusion Metallurgical Processes, MSFC-SPEC-3717 EM 20 MSFC Technical Standard, National Aeronautics and Space Administration, 2017.
[41] E. Malekipour, H. El-Mounayri, Common defects and contributing parameters in powder bed fusion AM process and their classification for online monitoring and control: a review, Int. J. Adv. Manuf. Technol. 95 (2018) 527–550.
[42] Y.J. Liu, S.J. Li, H.L. Wang, W.T. Hou, Y.L. Hao, R. Yang, T.B. Sercombe, L.C. Zhang, Microstructure, defects and mechanical behavior of beta-type titanium porous structures manufactured by electron beam melting and selective laser melting, Acta Mater. 113 (2016) 56–67.